UCSF
UC San Francisco Previously Published Works

Title

NIR-II-excited off-on-off fluorescent nanoprobes for sensitive molecular imaging in vivo.

Permalink

https://escholarship.org/uc/item/0xv315bn

Journal

Nature Communications, 16(1)

Authors

Tang, Yufu

Li, Yuanyuan

He, Chunxu

et al.

Publication Date

2025-01-02

DOI

10.1038/s41467-024-55096-y

Peer reviewed

NIR-II-excited off-on-off fluorescent nanoprobes for sensitive molecular imaging in vivo

Yufu Tang[1], Yuanyuan Li[2], Chunxu He[2], Zhen Wang[2], Wei Huang[2], Quli Fan [2] ✉ & Bin Liu [1] ✉

Strong background interference signals from normal tissues have significantly compromised the sensitive fluorescence imaging of early disease tissues with exogenous probes in vivo, particularly for sensitive fluorescence imaging of early liver disease due to the liver's significant uptake and accumulation of exogenous nanoprobes, coupled with high tissue autofluorescence and deep tissue depth. As a proof-of-concept study, we herein report a near-infrared-II (NIR-II, 1.0-1.7 μm) light-excited "off-on-off" NIR-II fluorescent probe (NDP). It has near-ideal zero initial probe fluorescence but can turn on its NIR-II fluorescence in liver cancer tissues and then turn off the fluorescence again upon migration from cancer to normal tissues to minimize background interference. Due to its low background, a blind study employing our probes could identify female mice with orthotopic liver tumors with 100% accuracy from mixed subjects of healthy and tumor mice, and implemented sensitive locating of early orthotopic liver tumors with sizes as small as 4 mm. Our NIR-II-excited "off-on-off" probe design concept not only provides a promising molecular design guideline for sensitive imaging of early liver cancer but also could be generalized for sensitive imaging of other early disease lesions.

Sensitive molecular imaging probes are highly desirable for early disease detection, optimizing therapeutic interventions, and personalized medicine[1–3]. Minimizing interference signals from non-target normal tissues is crucial to improve imaging sensibility with exogenous probes. A major trend in minimizing normal tissue signals is to develop "off-on" probes (also known as activatable probes or turn-on probes) that stay in the "off" state in the beginning and amplify their signals ("on" state) in disease tissues. To some extent, such "off-on" probes could reduce the normal tissue signal compared to traditional "always-on" probes (path 1 in Fig. 1a and b)[4–7]. However, once activated within the targeted disease tissues, these "off-on" probes were transitioned into "always-on" probes, emitting signals continuously even as they migrated from tumor to normal tissues (path 2 in Fig. 1b), thereby still generating significant normal tissue signals[1,8–11]. Indeed, robust

signals from normal tissues are frequently observed in practice for most existing "off-on" probes[12–17], which could cause false positive or negative diagnosis results[1]. The situation could be especially serious for livers owing to their central role in the uptake and accumulation of abundant exogenous nanoprobes[18].

Off-on-off" probes, staying in the "off" state at the beginning, amplifying signals in disease tissues ("on" state) in response to molecules of interest and then turning off signals ("off" state) upon migration from the disease tissues to normal tissues (path 2 in Fig. 1c), represent a more practical and effective approach to minimize the normal tissue signal compared with "off-on" probes[4,19–24]. This strategy could achieve a lower normal tissue signal interference, thus improving sensitive imaging performance in vivo. Among various imaging modalities, fluorescence imaging exhibits tremendous potential due to

[1]Department of Chemical and Biomolecular Engineering, National University of Singapore, 4 Engineering Drive 1, Singapore 117585, Singapore. [2]State Key Laboratory of Organic Electronics and Information Displays & Institute of Advanced Materials (IAM), Nanjing University of Posts & Telecommunications, 9 Wenyuan Road, Nanjing 210023, China. ✉e-mail: iamqlfan@njupt.edu.cn; cheliub@nus.edu.sg
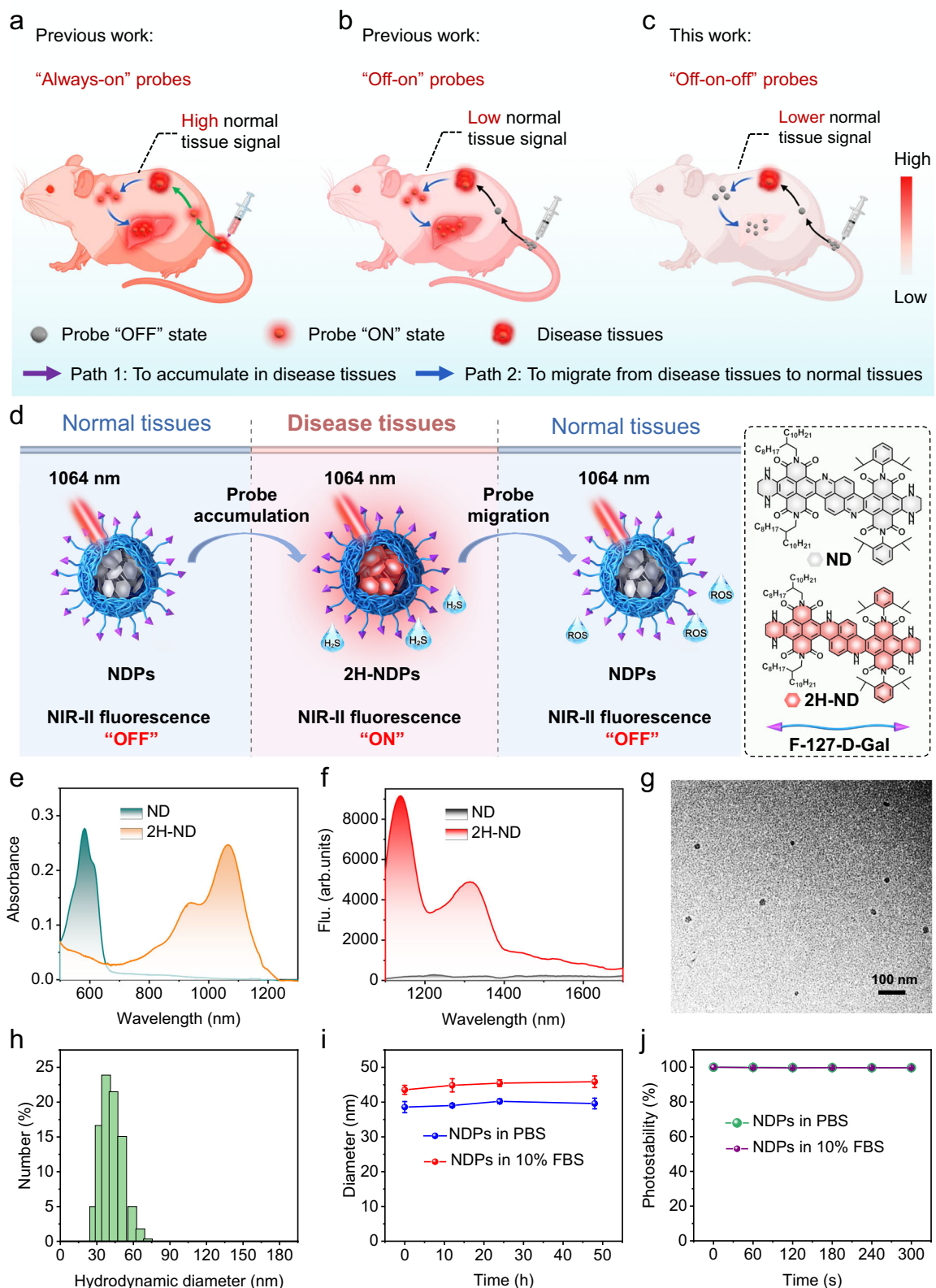
Fig. 1 | Design, sensing mechanism, and characterization of NDPs. Schematic illustration of normal tissue signal of previous works, showcasing (**a**) "always-on" probes and (**b**) "off–on" probes (also known as activatable probes or turn-on probes), and (**c**) this work "off-on-off" probes in vivo. Created in BioRender. Jiajing, G. (2022) BioRender.com/m53h190. **d** Schematic illustration of low background signal of NIR-II-excited "off-on-off" NIR-II fluorescent probes (NDPs) in vivo. Created in BioRender. Jiajing, G. (2022) BioRender.com/m53h190. **e** The absorption spectra of ND (1×10^{-6} M) and 2H-ND (1×10^{-6} M) in tetrahydrofuran. (**f**) The fluorescence spectra of ND and 2H-ND in tetrahydrofuran under 1064 nm excitation. Representative (**g**) transmission electron microscopy (TEM) and (**h**) dynamic light scattering (DLS) images of NDPs. The (**i**) structure stability and (**j**) photostability (power density of 2 W cm^{-2}) of NDPs. ($n = 3$ independent samples; mean ± SD).

its unique features, such as noninvasiveness, high sensitivity, excellent spatiotemporal resolution, real-time analysis, and localization of biomolecules at molecular levels[25]. However, the current main design principles to control probe fluorescence "off" and "on" change are based on photophysical processes to quench and revive fluorescence[4,19–21,23,26,27], such as aggregation-induced emission[28], photoinduced electron transfer[20,22,26], and fluorescence Förster resonance energy transfer[21,29]. Unfortunately, such photophysical processes usually cannot completely quench the fluorescence to achieve near-ideal zero initial probe fluorescence (ideally zero), which generates relatively high normal tissue signal from the probes distributed in normal tissues, especially for the liver with high uptake and accumulation of exogenous probes, thereby compromising in vivo imaging sensitivity[18]. By contrast, the design principle based on the change of fluorophore structure together with a large absorption redshift from a short wavelength (ideal zero absorption at the long excitation wavelength) to a long wavelength (robust absorption at the long excitation wavelength) after activation could be more advantageous. The probe activation associated with absorption change offers an additional advantage to use long-wavelength excitation to achieve a near-ideal zero initial probe signal and enhance the turn-on ratio to boost imaging sensibility[30]. Although several probes are based on the change of fluorophore structure together with a large absorption peak redshift to control probe fluorescence "off" and "on" change[4,31], the excitation or the emission wavelengths of most of these probes are within the traditional NIR-I (650–900 nm) window, exhibiting limited penetration depth and strong tissue autofluorescence[25]. The emerging second near-infrared window (NIR-II; 1000–1700 nm) fluorescence imaging permits real-time visualization of deep anatomical features with unprecedented spatial resolution[7,25,32–35]. Furthermore, it is better to use NIR-II excitation so that probes can achieve higher maximum permission exposure and deeper tissue penetration than NIR-I excitation[25]. However, to our knowledge, there are currently few NIR-II-excited "off-on-off" NIR-II fluorescent probes, not to mention NIR-II-excited "off-on-off" NIR-II fluorescent probes with near-ideal zero initial probe fluorescence. In fact, such probes hold particular significance for imaging of orthotopic disease tissue like livers due to their deep tissue depth and strong tissue autofluorescence[11,36–43].

To demonstrate our concept, hydrogen sulfide (H$_2$S), the third gaseous signaling molecule, was selected as an example biomarker in liver diseases due to its role as the initial response in conditions like inflammation, hepatic cirrhosis, and liver cancers, providing a promising avenue for early sensitive imaging[44,45]. Meanwhile, H$_2$S-involved liver cancer is used as one example of a disease model because sensitively identifying and localizing early liver cancer is a great challenge[45]. In fact, the clinical symptoms of early liver cancer are not obvious, and 50% of liver cancer patients are already in the advanced stage when diagnosed.

Herein, as a proof-of-concept study, we report naphthalene diimide derivative (ND)-based 1064 nm-excited "off-on-off" NIR-II fluorescent probes (NDPs) with near-ideal zero initial probe fluorescence to minimize normal tissue interference signals for sensitive imaging of early orthotopic liver tumor in vivo (Fig. 1d). To endow ND dyes with water-dispersity and tumor targeting effect to orthotopic HepG2 liver tumor, F-127-D-Gal is designed to encapsulate the dyes to form NDPs. The probe NDPs show near-ideal zero initial probe fluorescence ("off" state) at the beginning and then turned on NIR-II fluorescence ("on" state 2H-NDPs) in liver tumor in response to high-level H$_2$S. Subsequently, the "on" state 2H-NDPs can be turned off NIR-II fluorescence ("off" state) by the low-level presence of reactive oxygen species (ROS) in normal tissues upon migration from the disease tissues to normal tissues, greatly reducing interference signals in normal tissues (Fig. 1d). In addition, the change of probe fluorophore structure in the presence of molecules of interest

together with a large absorption redshift offers near-ideal zero initial probe fluorescence upon excitation at 1064 nm, which not only further reduces the normal tissue signals but also realizes an ultrahigh turn-on/off ratio (~12000-fold) and an ultralow H$_2$S detection limit (5 nM). As a proof of concept, NDPs can accurately screen animal patients with orthotopic liver tumors in a blind study and offer highly sensitive imaging of early orthotopic liver tumors with a small size of ~4 mm. Our probe design concept not only provides a promising molecular design guideline for sensitive identification and imaging of the early H$_2$S-involved lesions, including liver cancer, but also can be generalized for sensitive identification, localization and therapy of the other early lesions.

Results

The design and preparation of NDPs
To achieve highly sensitive tumor imaging in vivo, minimizing background signals in non-target normal tissues is crucial. H$_2$S, a highly reactive endogenous signaling molecule, can act as a strong reductant (the oxidation potential $Eox = -0.476$ V) to donate two electrons to maintain redox homeostasis and detoxify xenobiotics in vivo[45]. Importantly, the H$_2$S level in malignant liver tumors is much higher than that in normal liver tissues, providing an exciting opportunity for the sensitive detection of early liver cancer[44–47]. Therefore, H$_2$S was chosen as the molecule of interest to turn on the NIR-II fluorescent signal for imaging early malignant liver tumors in this study. So far, most of the developed H$_2$S-responsive probes (Supplementary Fig. S1)[48–52] are"off-on" and difficult to offer completely dark initial probe fluorescence and ultra-high turn-on ratios. Herein, an H$_2$S-responsive NIR-II fluorescent small molecule (ND) was designed and synthesized based on naphthalene-diimide dye[53]. The ND was achieved by broadening the conjugated skeleton of naphthalene-diimide dye to shift its absorption and emission peaks into the NIR-II window (Fig. 1d and Supplementary Fig. S2). In ND, the 2,6-diisopropylaniline groups were crucial to increase intermolecular space in water. The density functional theory (DFT) calculations revealed an 84.2° dihedral angle between the 2,6-diisopropylaniline group and naphthalene-diimide at the optimized ground state (Supplementary Fig. S3). Such a large dihedral angle can not only weaken the molecular aggregation of ND in water, but also enhance the accessibility of analytes (e.g., H$_2$S or ROS) to ND.

Next, the optical property of ND in organic solvent was tested. As shown in Fig. 1e, ND shows a major absorption peak at around 585 nm with no absorption beyond 1000 nm in tetrahydrofuran (THF). However, 2H-ND, the H$_2$S reduction product of ND, exhibits an absorption maximum at 1066 nm. Upon excitation at 1064 nm, ND shows no NIR-II emission (Fig. 1f). However, 2H-ND shows a major emission peak at 1138 nm and a shoulder at 1316 nm (Fig. 1f).

The general requirements of efficient probes include good biocompatibility, excellent water dispersibility, and strong tumor-targeting capability. A D-galactose (D-Gal)-conjugated amphiphilic F-127 polymer (F-127-D-Gal) was synthesized (Fig. 1d and Supplementary Fig. S2) and used to encapsulate ND molecules to form nanoprobes (NDPs) via a modified nanoprecipitation method using a coaxial microfluidic glass capillary mixer (Supplementary Fig. S4). D-Gal group was used to enhance endocytosis to increase the probe-target activity for liver tumors due to its specific interaction with liver cancer HepG2 cell-overexpressed galactose receptor asialoglycoprotein[47,54–56]. NDPs have spherical morphology (Fig. 1g) in TEM with a size of 40 nm, which is similar to that of DLS measurement (Fig. 1h). Meanwhile, NDPs were stable during storage in PBS buffer (pH 7.4) and 10% FBS at 37 °C for 48 h (Fig. 1i). Almost no photobleaching was observed when NDPs were exposed to a 1064 nm laser upon irradiation at a high-power density of 2 W cm^{-2} for 5 min (Fig. 1j). These results demonstrate that NDPs are suitable for in vivo imaging.
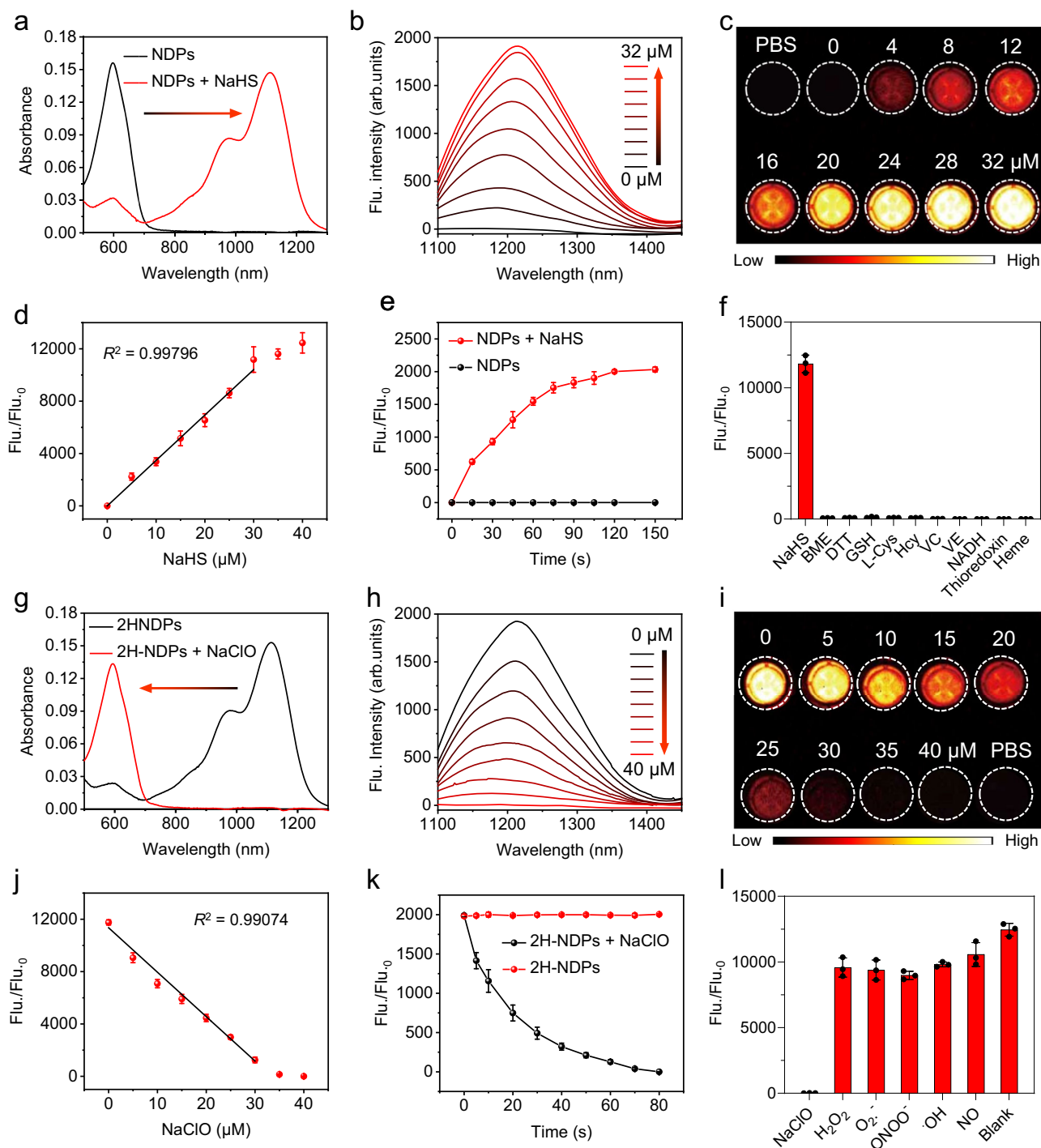
Fig. 2 | In vitro "off-on-off" responses of probes for H$_2$S and ROS. All experiments were performed with 10 μg mL^{-1} NDPs or 2H-NDPs in PBS (1 mM, pH 7.4) at 37 °C. All 2H-NDP solution (10 μg mL^{-1}) was achieved by the addition of the H$_2$S (32 μM) to the NDP solution (10 μg mL^{-1}). Absorption spectra of (**a**) NDPs and (**g**) 2H-NDPs before and after incubation with their respective analytes (32 μM NaHS or 40 μM NaClO). NIR-II fluorescence spectra changes of (**b**) NDPs and (**h**) 2H-NDPs, as well as their corresponding NIR-II fluorescence images of (**c**) NDPs and (**i**) 2H-NDPs upon treatment with their respective analytes NaHS (0 – 32 μM) or NaClO (0 – 40 μM) following excitation at 1064 nm. The plot of the Flu./Flu$_0$ (where Flu$_0$ indicates the fluorescence intensity of the NDPs at 1216 nm without NaHS and Flu. is the fluorescence intensity of NDPs or 2H-NDPs at 1216 nm in the presence of different concentrations of their respective analytes NaHS or NaClO, respectively) of (**d**) NDPs and (**j**) 2H-NDPs (n =3 independent samples; mean ± SD). The time-dependent Flu./Flu$_0$ of the (**e**) NDPs and (**k**) 2H-NDPs upon addition of their respective analytes (n = 3 independent samples; mean ± SD). The Flu./Flu$_0$ of (**f**) NDPs and (**l**) 2H-NDPs toward their respective analytes (n = 3 independent samples; mean ± SD).

In vitro "off-on-off" responses of probes to H$_2$S and ROS

The optical sensing of NDPs for H$_2$S was first evaluated in vitro. The NDPs exhibited a major absorption peak at around 596 nm with no absorption beyond 800 nm (Fig. 2a). To mimic the H$_2$S environment in a living system, NaHS was used as the H$_2$S donor, which can rapidly release H$_2$S gas in water[45]. Upon addition of NaHS, NDPs showed a significant reduction in the absorption peak at ~596 nm, and a absorption peak appeared at 1112 nm with an isosbestic point of

700 nm (Fig. 2a) with an ε of $5.0 \times 10^5 M^{-1} cm^{-1}$ (Supplementary Fig. S5). Such a large redshift (516 nm) of absorption peak was attributed to H_2S-induced fluorophore structure change from ND to 2H-ND in NDPs. Along with the absorption change, the suspension color was changed from blue to brownish-black (Supplementary Fig. S6). The NaHS concentration-dependent NIR-II emission spectra for NDPs were recorded in PBS (pH = 7.4) at 37 °C (Fig. 2b). As NDPs exhibited no absorption beyond 800 nm, the initial probe fluorescence intensity (without the addition of NaHS) was near-ideal zero under 1064 nm laser excitation (Fig. 2b). After the addition of NaHS from 0 – 32 μM, the NIR-II emission of NDPs was gradually enhanced upon 1064 nm excitation and the maximum emission wavelength was at 1216 nm (Fig. 2b) with an NIR-II fluorescence quantum yield of 0.03% (measured using IR-26 (quantum yield = 0.05%)[18,57–59] as a reference) in water (Supplementary Fig. S7). Thanks to the near-ideal zero initial probe fluorescence intensity, the NDPs exhibited a ~12000-fold fluorescence turn-on ratio in response to NaHS.

Next, the NIR-II fluorescence images (1100–1700 nm) of the NDPs in PBS solutions at different concentrations of NaHS were further recorded in pseudo-red hot through a small living animal NIR-II fluorescence imaging system (Fig. 2c). As shown in Fig. 2c, the blank fluorescence intensity of pure PBS solution was similar to that of the initial probe fluorescence intensity (0 μM NaHS), which indicates that initial probe fluorescence intensity of NDPs was near-ideal zero. NIR-II fluorescence images of NDPs showed that NIR-II fluorescence (pseudo-red hot) gradually intensified with the increase of NaHS concentration (Fig. 2c). A linear trend ($R^2 = 0.9979$) was observed with increasing NaHS concentration from 0 to 32 μM (Fig. 2d). The limit of detection (3σ/k) for NDPs toward NaHS was determined to be ~5 nM, which was sufficient for in vivo imaging of tumor H_2S[45]. Additionally, the reaction kinetics of NDPs showed a rapid response for NaHS, and the reaction was completed within 90 s (Fig. 2e), providing the possibility of real-time imaging in vivo. The selectivity of NDPs toward NaHS was studied by monitoring the NIR-II fluorescence change at 1216 nm after treatment with various suspected analytes (1 mM), including β-mercaptoethanol (BME), dithiothreitol (DTT), glutathione (GSH), L-cysteine (L-Cys), homocysteine (Hcy), vitamin C (VC), Vitamin E, NADH (Nicotinamide Adenine Dinucleotide), Thioredoxin, and Heme. The NDPs exhibited an obvious increase in their NIR-II fluorescence after being treated with H_2S, but not in the presence of other biologically relevant analytes (Fig. 2f), indicating its high selectivity for H_2S. Meanwhile, the fluorescence turn-on ratio of NDPs toward H_2S was also unaffected by the change in physiological pH (4.0–9.0) (Supplementary Fig. S8) and temperature (29 – 45 °C) (Supplementary Fig. S9). Therefore, NDPs are expected to offer low background, good specificity, and high sensitivity for tumor imaging in vivo.

We then investigated the NIR-II fluorescence sensing capability of 2H-NDPs for ROS in vitro. The 2H-NDPs were achieved by the addition of the H_2S to the NDPs. We first chose sodium hypochlorite (NaClO) as a representative ROS to study how it can change the probe optical properties. Upon addition of NaClO, 2H-NDPs showed a significant reduction in the absorption peak at 1112 nm until close to zero, together with an increase of the absorption peak at 596 nm (Fig. 2g), which is the reverse process for NaHS response. Meanwhile, the brownish-black solution of 2H-NDPs was changed into blue again following the NaClO administration (Supplementary Fig. S10). As expected, the NIR-II emission at 1216 nm is gradually attenuated to near-ideal zero upon titration with NaClO (Fig. 2h). Correspondingly, the NIR-II fluorescence intensity (pseudo-red hot) of the 2H-NDPs in PBS solutions gradually reduced with increased NaClO concentration until it reached the same as that of the pure PBS solution (Fig. 2i). The detection limit (3σ/k) for 2H-NDPs against NaClO was 8 nM (Fig. 2j). The kinetics of NaClO-induced NIR-II fluorescence attenuation was completed within 80 s (Fig. 2k). In addition to NaClO, other oxidizing species, such as H_2O_2, $ONOO^-$ and ·OH, could also reduce the fluorescence of 2H-NDPs to a

certain extent (Fig. 2l). This will reduce tumor-activated probes (2H-NDPs) when they are migrated to normal tissues. The change in fluorescence of 2H-NDPs in response to NaClO was not sensitive at physiological pH (4.0–9.0) (Supplementary Fig. S11) and temperature (29 – 45 °C) (Supplementary Fig. S12), indicating that NDPs can be applied in a complex and dynamic physiological environment in a living body.

Off-on-off" mechanism and ability of NDPs
To understand the "off-on-off" mechanism, we performed in situ ^{1}H NMR spectrum analysis to confirm the structure of the primary redox sensing component ND. As shown in Fig. 3, upon addition of an aqueous solution of NaHS in tetrahydrofuran-D_8, the intensity of the secondary amine protons (denoted as "e" in Fig. 3a) in the middle of a 2H-ND molecule at 12.5 ppm gradually increased owing to the release of free secondary amine proton. On the contrary, the intensity of the He proton of 2H-ND at 12.5 ppm was gradually decreased upon NaClO treatment. The chemical shift of the secondary amine protons (denoted as "a" in Fig. 3a) on both sides of the molecule remains unchanged either by treatment with NaHS or NaClO, indicating that these secondary amine protons remain constant in the "off-on-off" response process. Next, mass spectroscopy showed that the molecular weight of ND was changed to that for 2H-ND in the presence of NaHS and then reverted back to ND upon further addition of NaClO (Supplementary Figs. S13–15). The results of absorption, fluorescence, ^{1}H NMR, and Mass spectroscopy data unambiguously supported the proposed "off-on-off" reaction mechanism that the meso-N was "off-on-off" between −N = C− and −NH−C− (Fig. 3a). Such a "off-on-off" structure change is the main reason for the switchable optical property of NDPs. Theoretical calculations were then carried out to delineate the origin of the particularly large-absorption change between ND and 2H-ND. Based on DFT analyses, both molecules possessed completely planar polycyclic skeletons upon energy minimization (Supplementary Fig. S16a). The LUMO of 2H-ND was nearly identical to that of ND. In contrast, the HOMO energy level of ND was considerably lowered relative to that of 2H-ND (Supplementary Fig. S16b). The smaller bandgap of 2H-ND agrees with its long wavelength absorption (Supplementary Fig. S16c).

Next, we investigated the dynamic "off-on-off" ability of NDPs in vitro and in vivo. As shown in Fig. 3b, NDPs in PBS in 96-well plates were added with NaHS and NaClO. The NaHS-induced NIR-II fluorescence increment could be turned "off" to nearly the initial value after the addition of NaClO (Fig. 3c). Subsequently, NIR-II fluorescence imaging of "off-on-off" ability in a living mouse was studied via intramuscular injection of NDPs in the right hind leg (Fig. 3d). The left hind leg was used as the control group where the same volume of PBS was injected simultaneously. As shown in Fig. 3e and Supplementary Fig. S17, the NaHS-induced NIR-II fluorescence "on" and NaClO-caused fluorescence "off" in the right hind leg of mice could be observed compared to that of the PBS group in the left hind leg. Taken together, NDPs could act as a reliable NIR-II probe for monitoring the redox dynamics both in vitro and in vivo.

In vivo investigation of the turn-off of 2H-NDP signal in normal tissue
In fact, the disease tissue-to-normal tissue signal ratio exceeding the Rose criterion, which states that a signal-to-background ratio of 5 is needed to distinguish image features with 100% certainty, signifies enough capability to differentiate disease tissues from healthy tissue with 100% certainty[60–63]. Although the ratio of many probes is greater than 5[6,12–17], most of them are proof-of-concept studies and have not paid much attention to high signals in normal tissues, which could cause false positive or negative diagnosis results in clinical practice. The high normal tissue signal is more prominent for the clinical application of some special tissues. For example, for liver tumor imaging in clinical practice, a ratio >2 is generally considered to be a
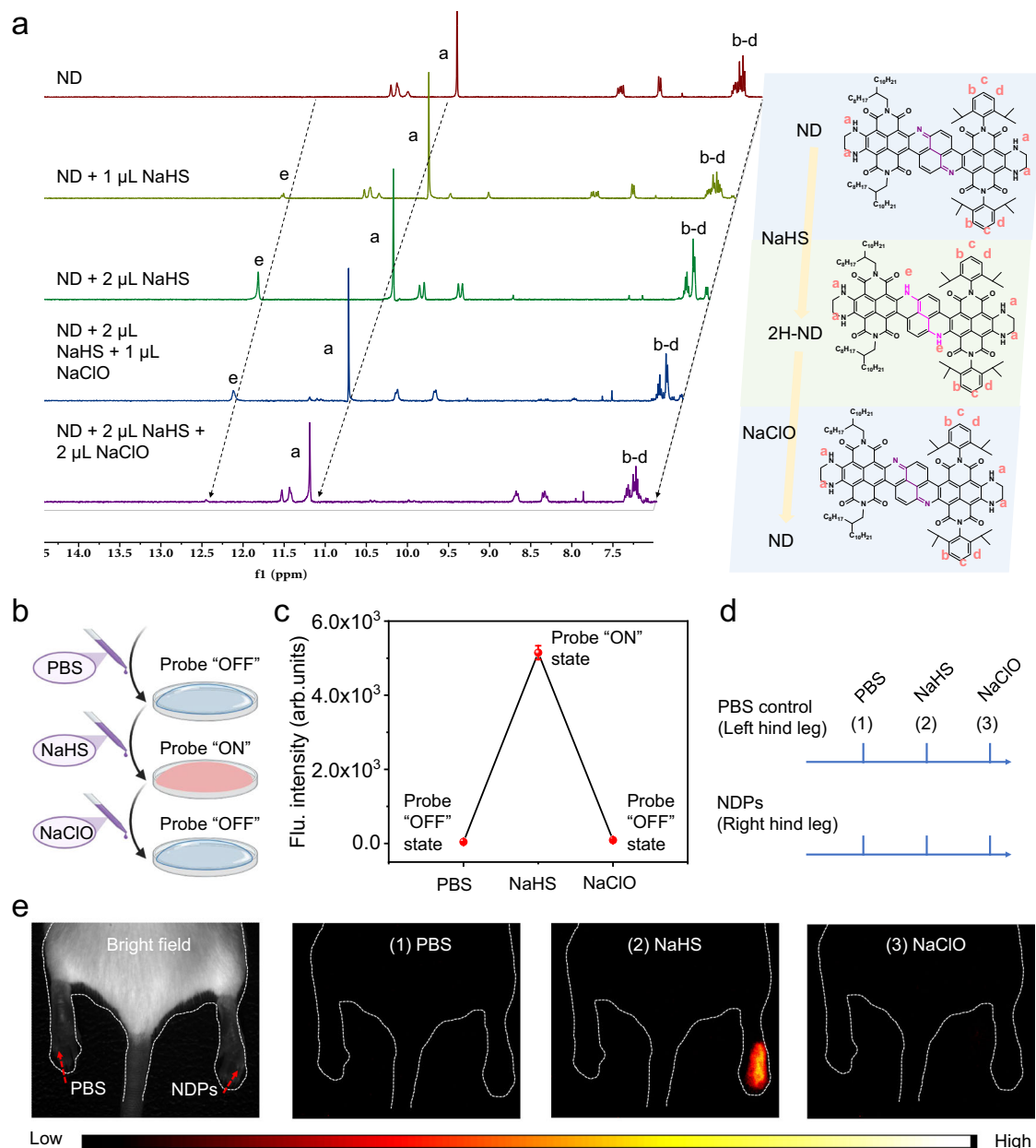
Fig. 3 | Off-on-off" mechanism of ND and cycle response evaluation of NDPs. **a** Partial ¹H NMR spectra monitoring of ND in the presence of NaHS and NaClO (1.2 equiv) in THF-D₈/water (v/v = 95/5). **b** Schematic illustration of the "off-on-off" NIR-II fluorescence evaluation of NDPs (5 μg mL⁻¹) in vitro. Created in BioRender. Jiajing, G. (2022) BioRender.com/m53h190. **c** Quantified NIR-II fluorescence intensity of (**b**) (*n* = 3 independent samples; mean ± SD). **d** Schematic illustration of the "off-on-off" NIR-II fluorescence evaluation of NDPs in mice. **e** In vivo NIR-II fluorescence images of NDPs (2 μg mL⁻¹, 10 μL) upon different treatments, *n* = 3 mice per group.

suspected liver tumor to identify as many early suspected tumor tissues as possible[64] because high signals of normal tissues can easily obscure early lesions, even if these tiny lesions genuinely exist but cannot be detected. Therefore, minimizing normal tissue signals is crucial for sensible imaging of early lesions. "Off-on" probes are currently the best strategy to improve molecular imaging sensibility in vivo by reducing normal tissue signals. The fate of intravenously injected "off-on" or "off-on-off" probes in vivo is divided into two processes: first, probes are continuously accumulated into the tumor followed by activation; second, these activated probes are subsequently migrated from the tumor into normal tissue, which is a dynamic process that happens all the time throughout the imaging. While the first process is the same for both "off-on" and "off-on-off" probes, in the second step, the activated products of any traditional

"off-on" probes, that is "always-on" probes, continuously emit signals even when they migrated into normal tissues. By contrast, the activated products of "off-on-off" probes could turn off their signal when they are migrated into normal tissues, which could obtain lower background signal than that of "off-on" probes. For our "off-on-off" probes (NDPs), the activated products (2H-NDPs) could return to NDPs in normal tissues to turn off their signal (Fig. 4a). Cell experiments also revealed that the activated probes (2H-NDPs) were indeed capable of migrating out of the tumor cells (Supplementary Fig. S18). To further prove our hypotheses that the second step of "off-on-off" probes could cause a lower background than that of "off-on" probes, that is, normal tissues could turn off the signal of 2H-NDPs, Me-H-ND with one methyl group blocking one of the two hydrogen reaction sites of 2H-ND was synthesized and encapsulated into F127-D-Gal to yield "always-on"
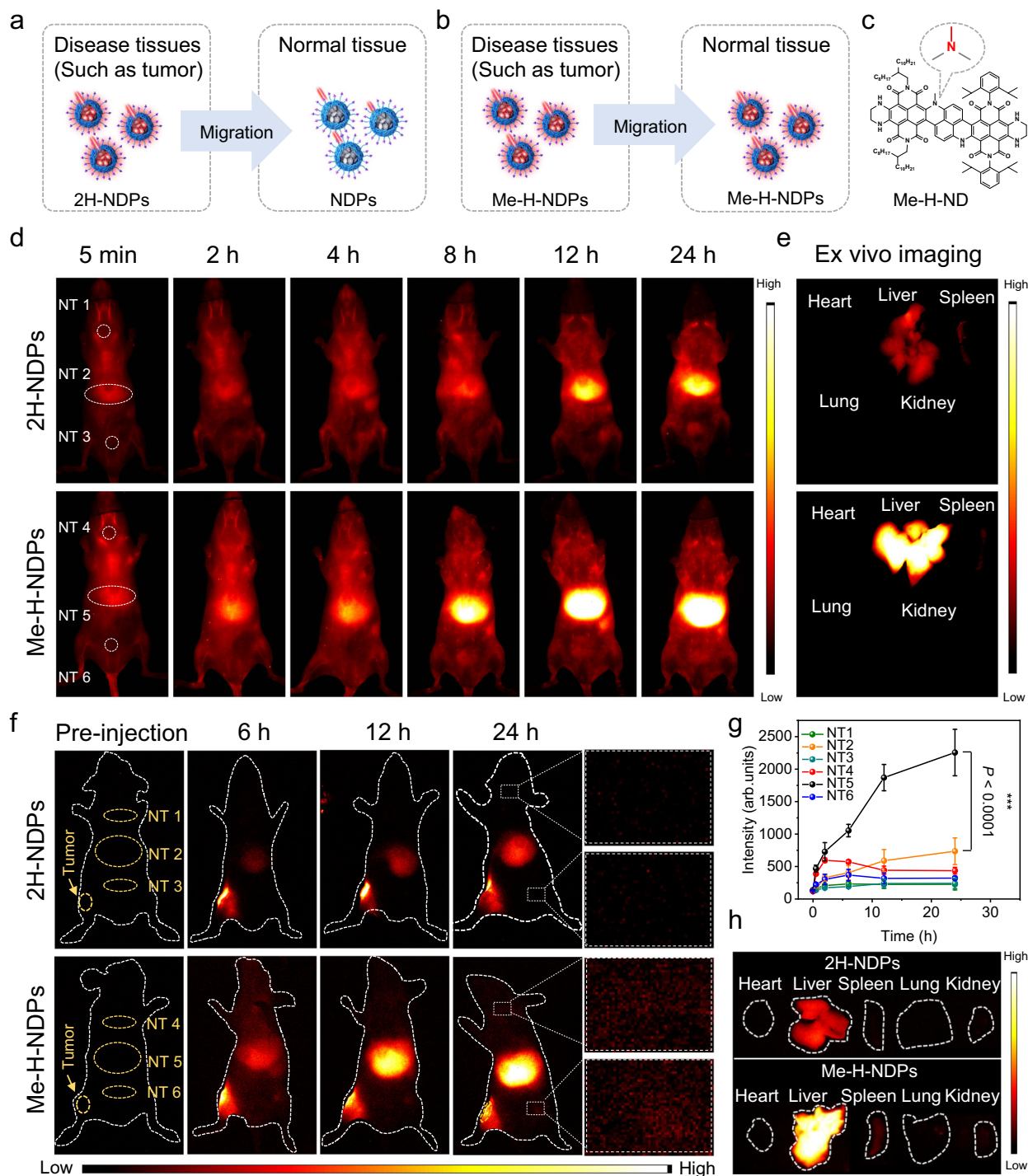
Fig. 4 | In vivo investigation of the turn-off of 2H-NDP signals in normal tissues. Schematic illustration of fluorescent signal change of the activated probe products of (**a**) "off-on-off" probes (2H-NDPs) and (**b**) control "off-on" probes (Me-H-NDPs) in living mice. Created in BioRender. Jiajing, G. (2022) BioRender.com/m53h190. **c** The chemical structure of Me-H-ND. (**d**) The representative in vivo NIR-II fluorescence images of 2H-NDPs (2 mg Kg^{-1}) and Me-H-NDPs (2 mg Kg^{-1}) in healthy mice, $n = 3$ mice per group. **e** Representative ex vivo NIR-II fluorescence images of main organs. (**f**) The representative in vivo NIR-II fluorescent images of mice following intratumoral injection of 2H-NDPs (0.8 mg mL^{-1}, 25 µL) and Me-H-NDPs (0.8 mg mL^{-1}, 25 µL), $n = 3$ mice per group. **g** Quantification of NIR-II fluorescence of ROI-1-6 of (**h**) at different times ($n = 3$ biologically independent samples; mean ± SD). $P < 0.0001$. Statistical significance was determined using one-way ANOVA. **h** Representative ex vivo NIR-II fluorescent images of main organs at 24 h post-injection.

probes (Me-H-NDPs) as a control (Fig. 4b and c). In addition, 2H-NDPs and Me-H-NDPs showed similar surface, shape, and average hydrodynamic size of 40 ± 1 nm (Fig. 1g and Supplementary Fig. S19). The fluorescence of Me-H-NDPs showed almost no change before and after the addition of ROS (Supplementary Fig. S20). Under 1064 nm

excitation, the fluorescence intensity of Me-H-NDPs is almost the same as that of 2H-NDPs at the same concentration (Supplementary Fig. S21). These results could largely rule out the differences in their biological distribution. Then, 2H-NDPs and Me-H-NDPs were intravenously injected into healthy mice, respectively. The normal tissue signal of the

control Me-H-NDPs in the whole body is higher than that of the 2H-NDPs group from 0 to 24 h post-injection (Fig. 4d and Supplementary Fig. S22a). Furthermore, NIR-II imaging of ex vivo major organs showed that the fluorescence of the liver for Me-H-NDPs was 3.2-fold higher than that of 2H-NDPs at 24 h post-injection (Fig. 4e and Supplementary Fig. S22b). These results indicate that the normal tissue could turn off the activated NIR-II fluorescence of 2H-NDPs. To further investigate the potential of normal tissues to transform 2H-ND into ND, 2H-NDPs and the control PBS were subcutaneously injected into the backs of healthy mice (Supplementary Fig. S23a). After 12 h, MALDI-TOF mass detection revealed a predominant molecular weight of ND (calculated m/z = 1674.28; found 1674.806) in liver tissues of the 2H-NDPs-treated mice (Supplementary Fig. S23b, c). This finding indicates that 2H-ND in the 2H-NDPs can indeed be converted into ND within normal tissues in vivo. Next, to investigate the effect of the migration process of 2H-NDPs from tumor to normal tissue, 2H-NDPs and the control Me-H-NDPs (0.8 mg mL^{-1}, 25 μL) were injected into the tumor of the sub-cutaneous HepG2 tumor-bearing mice. The fluorescence of 2H-NDPs and the control Me-H-NDPs gradually increased in the whole body from 0 to 24 h post-injection, which could be attributed to the probe migration from the tumor into the whole body (Fig. 4f, g). As expected, the fluorescent signals of Me-H-NDPs in normal tissues, especially for the liver (normal tissue (NT) 5 in Fig. 4g), are significantly stronger than that of the 2H-NDPs group at the same time point (NT2 in Fig. 4g). Even after 24 h following the injection of the probe, the fluorescence intensity in the normal tissues (NT 4 and NT 6) of the Me-H-NDPs group is still ~2-fold as high as that observed in the 2H-NDPs group (NT 1 and NT 3) (Fig. 4f, g). To further study the background signal intensity on major organs, mice were sacrificed and NIR-II imaging of ex vivo major organs showed that 2H-NDPs exhibited lower fluorescence brightness compared with Me-H-NDPs (Fig. 4h). More importantly, the fluorescence of the liver for 2H-NDPs was far lower (as low as 3.98-fold) than that of Me-H-NDPs (Fig. 4h and Supplementary Fig. S24). Next, we further investigated the biodistributions of ND and Me-H-ND in the muscles and livers using a classic method[65]. The concentrations of 2H-NDPs and Me-H-NDPs are comparable in muscle or liver, respectively, Supplementary Fig. S25, which indicates that the stronger fluorescence in Me-H-NDPs-treated mice is not due to the higher concentration of Me-H-NDPs. All studies verified our hypothesis that 2H-NDPs, the products of NDPs activation in the tumor, could turn off their NIR-II fluorescent signal in normal tissues to yield a low background signal. In vitro experiments in Fig. 2g-l indicated that ROS, including H_2O_2, HO•, $O_2^{•-}$, OCl^- and $ONOO^-$, et al., were crucial to reduce the NIR-II fluorescent signal of 2H-NDPs. Indeed, some normal tissues, such as livers, generate medium levels of ROS[66–68]. For example, the normal concentration of an intracellular H_2O_2 level in vivo is ~0.5×10^{-7}–7×10^{-7} M[25]. The average level of HClO generation from neutrophils under physiological conditions is about 0.47 nmol min^{-1} per 10^6 cells[25]. The physiological concentration of HClO in normal tissues is about 5–25 μM[69–71]. Basal production rate of $ONOO^-$ in physiological steady-state concentration is 0.1×10^{-6}–1×10^{-6} M min^{-1}[125]. These strong oxidizing ROS can oxidate 2H-NDPs into NDPs to reduce the normal tissue signal. By contrast, the H_2S productions of mouse normal colon muscle, brain and liver tissues are about 8 pmol/min/mg tissue, 7 pmol/min/mg tissue and 20 pmol/min/mg tissue, respectively[72–74].

Additionally, the autofluorescence of biological tissue often contributes to a high normal tissue signal[75,76]. Currently, the excitation wavelength of most NIR-II fluorescent probes is below 1000 nm, which suffers from serious autofluorescence of biological tissues. Fortunately, the activated NDPs (2H-NDPs) showed strong absorption at ~1100 nm (Fig. 2a). To verify that the longer wavelength excitation could lead to lower autofluorescence, the tissue images upon excitation at 1064 and 808 nm were compared (Supplementary Fig. S26). The average autofluorescence of the whole body for 808 nm excitation was ~3.1-fold higher than that of 1064 nm excitation under the same

laser power and on the same mice. More seriously, the auto-fluorescence in the liver under 808 nm excitation was up to 5.4-fold higher than that of 1064 nm excitation. Consequently, NIR-II excitation effectively reduced the non-target normal tissue signal from tissue autofluorescence.

NIR-II fluorescence imaging of H_2S and subcutaneous liver tumors

Firstly, the targeting ability of D-Gal on the surface of NDPs for HepG2 cells is studied. The NIR-II fluorescence of the NDPs with D-Gal group in HepG2 cells is stronger than that of the no D-Gal group (Supplementary Fig. S27). In addition, HepG2 cells show higher uptake than that of normal cells, such as 3T3 and HEK 293 T cells (Supplementary Fig. S28). Furthermore, the NIR-II fluorescence of the 2H-NDPs with D-Gal group in HepG2 tumor of tumor-bearing mice is also stronger than that of F-127-NDPs with no D-Gal group (Supplementary Fig. S29). These data indicate that D-Gal has a high targeting ability. Next, we first examined the imaging capabilities and specific response efficacy in tumor HepG2 cells (Supplementary Fig. S30). Compared with NDPs-treated HepG2 cells, the NIR-II fluorescence significantly increased when pre-treated with extraneous NaHS. Conversely, pre-treatment with $ZnCl_2$, which scavenges H_2S, markedly reduced the NIR-II fluorescence. Stimulating HepG2 cells with L-Cys, a precursor for H_2S biosynthesis, resulted in enhanced NIR-II fluorescence, which was significantly diminished by the addition of NaClO to suppress the NIR-II fluorescence. These findings show that NDPs show H_2S-specific responses. In vivo blood elimination kinetic study indicates that the blood half-life of NDPs was up to ~10 h (Supplementary Fig. S31). Such a long half-life could facilitate efficient circulation to deliver NDPs into tumor tissues. To further investigate the tumor imaging capability of NDPs in vivo, NDPs (10 mg Kg^{-1}) were intravenously injected into nude mice bearing sub-cutaneous HepG2 tumor xenografts (Fig. 5a). As shown in Fig. 5b, NIR-II fluorescent signals in the tumor were increased gradually over time, indicating their successful tumor accumulation and subsequent fluorescence activation.

The 1064 nm-excited NIR-II fluorescence imaging exerted a significantly high tumor-to-normal tissue (T/NT) signal ratio (Fig. 5c). The average T/NT of NDPs was 31.22 at 12 h post-injection, substantially higher than the Rose criterion[7] (red dashed line in Fig. 5c, with a T/NT ratio of 5 required to distinguish image features with 100% certainty). More importantly, the T/NT ratio with NDPs above the Rose criterion started from 1 h post-injection, which lasted for 12 h. The long duration of the T/NT ratio above the Rose criterion should benefit better precise tumor identification and surgical excision in clinical practice. To further confirm the H_2S specificity of NDPs in vivo, L-Cys and aminooxy-acetic acid (AOAA) were injected into the tumor to upregulate and scavenge H_2S levels[45,77]. As shown in Fig. 5b and c, AOAA treatment led to reduced NIR-II fluorescence, whereas the fluorescence is intensified from tumors upon treatment with L-Cys. The T/NT ratio at 12 h post-injection of NDPs of L-Cys-treated mice is ~1.6-fold and ~3.4-fold higher than that of NDPs alone and mice pretreated with H_2S scavenger AOAA, respectively. These results indicate that NDPs could respond to H_2S in vivo. Thus, the contrast increase could be associated with the signal amplification after NDPs activation in the presence of a high H_2S level in tumor tissues.

Application of NDPs in a blind study of mice with orthotopic liver tumors

To prove that the designed "off-on-off" probes (NDPs) has low signals in normal tissue, we prepared "off-on" probes (2S-NDPs) as a control (Fig. 6a, b). 2S-NDPs were achieved through nanoprecipitation with F127-D-Gal to encapsulate 1,4-bis(methylsulfanyl)benzene (2S-Ph) and ND in a molar ratio of 2 (Fig. 6b). 2S-Ph shields the reaction between ND and ROS because the small-sized 2S-Ph is present in large excess within the nanoparticles (2S-NDPs), forcing ROS to react with two sulfur
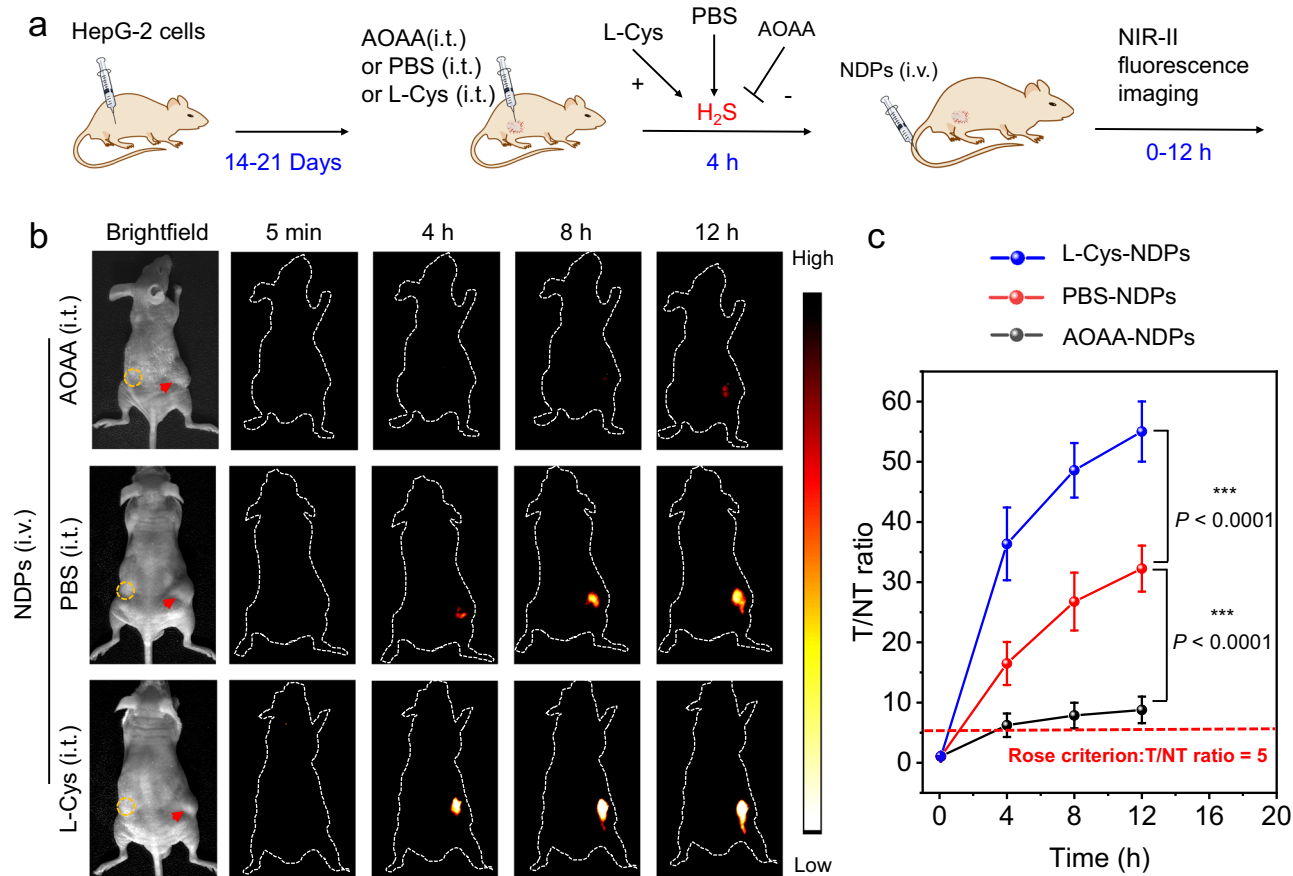
Fig. 5 | NIR-II fluorescence imaging of H₂S in subcutaneous liver tumors.
a Schematic for NIR-II fluorescence imaging of H_2S in HepG2 tumor-bearing mice. Created in BioRender. Jiajing, G. (2022) BioRender.com/m53h190. **b** NIR-II fluorescence imaging of tumors in mice at 5 min, 4, 8, and 12 h following intravenous injection (i.v.) injection of NDPs (2 mg Kg⁻¹) in PBS, NDPs (2 mg Kg⁻¹) with intratumoral injection (i.t.) injection of H₂S enhancer (L-Cys) or scavenger (AOAA). ($n = 3$ mice per group). L-Cys (1 mM, 25 μL) or AOAA (1 mM, 25 μL) was injected into tumors at 4 h before i.v. injection of NDPs. Red arrows indicate the locations of HepG2 tumors in mice, and yellow circles indicate the locations of normal tissues. **c** A comparison of the T/N contrast ratio after the administration of L-Cys-NDPs, PBS-NDPs, and AOAA-NDPs ($n = 3$ biologically independent samples; mean ± SD). $P < 0.0001$. Statistical significance was determined using one-way ANOVA.

atoms of 2S-Ph[78–80] first upon attacking the nanoparticles[79]. Consequently, 2S-NDPs function as "off-on" probes in contrast to the "off-on-off" behaviour of NDPs. As depicted in Supplementary Fig. S33, 2S-Ph minimally impacts the reaction between H₂S and ND but could block the reaction between ND and ROS. Furthermore, 2S-NDPs exhibit similar average hydrodynamic diameters (45 nm) and a typical spherical morphology (Supplementary Fig. S33) as NDPs.

In clinical practice for cancer diagnosis, the primary objective of medical imaging was to screen cancer patients from suspected people, then locate the tumor and reveal the anatomical features of cancer tissues. To simulate clinical practice for screening cancer patients, we designed a blind study to evaluate how NDPs can be used to identify cancer animals with orthotopic liver tumors based on H₂S levels. Firstly, we used four healthy mice to establish a diagnostic threshold based on their NIR-II fluorescence change (Flu.Final/Flu.Initial). Flu.Final and Flu.Initial are the NIR-II fluorescence intensities in the liver at 10 h and 0 h post i.v. injection of NDPs, respectively. The Flu.Final/Flu.Initial values of four healthy mice at 10 h post i.v. injection of NDPs are 1.98, 2.56, 2.13, and 1.86, respectively, which yielded a value of 2.13 ± 0.31 (mean value + s.d.) (Fig. 6c). As the diagnostic threshold (2.75) was defined as the mean (2.13) adding 2-fold of the s.d. value (0.31)[81,82], once the Flu.Final/Flu.Initial value of a mouse is >2.75, it is not a healthy mouse but a suspected cancer patient. This offers a great opportunity to conduct a blind study to screen cancer animals with orthotopic liver tumors based on the H₂S levels. We utilized two separate batches of mice from different time points to mitigate any potential batch effects.

Each batch is consisted of six mice, and identical procedures were applied to both batches. Three nude mice in each batch were inoculated with HepG2 cells in their livers. The other three mice in this batch were treated with the same process except using normal saline instead of HepG2 cells to ensure no biasing of the results based on the appearance of these six mice in the same batch. These two batches of mice were tagged but with no deviation in appearance (Fig. 6d). After 15 days, the two batches were passed to an imaging diagnostician. The identity of these mice was blind to the imaging diagnostician until completion of the study. NDPs were intravenously injected into these two batches of mice by the imaging diagnostician to perform NIR-II whole-body fluorescence imaging. Meanwhile, another three confirmed orthotopic liver tumor mice were prepared with the above method and then were intravenously injected with 2S-NDPs to perform NIR-II whole-body fluorescence imaging. As shown in Fig. 6e, the imaging results for the first batch of six mice were shown as mice numbered Batch (B)1-1, B1-2, B1-3, B1-4, B1-5 and B1-6, while the imaging results of the second batch of six mice were shown as mice numbered B2-1, B2-2, B2-3, B2-4, B2-5 and B2-6. For the first batch of six mice, the NIR-II fluorescence of the B1-2, B1-3, B1-6 mice in liver tissues was significantly brighter than that of the B1-1, B1-4, B1-5 mice. In the second batch, the B2-1, B2-3, and B2-5 mice exhibited significantly stronger signals than the B2-2, B2-4, and B2-6 mice. Correspondingly, the Flu.Final/Flu.Initial values of the B1-2, B1-3, B1-6 mice in the first batch, as well as B2-1, B2-3, B2-5 mice in the second batch, were 23.44, 20.87, 20.09, 26.38, 25.27 and 21.69, respectively, which were much stronger than
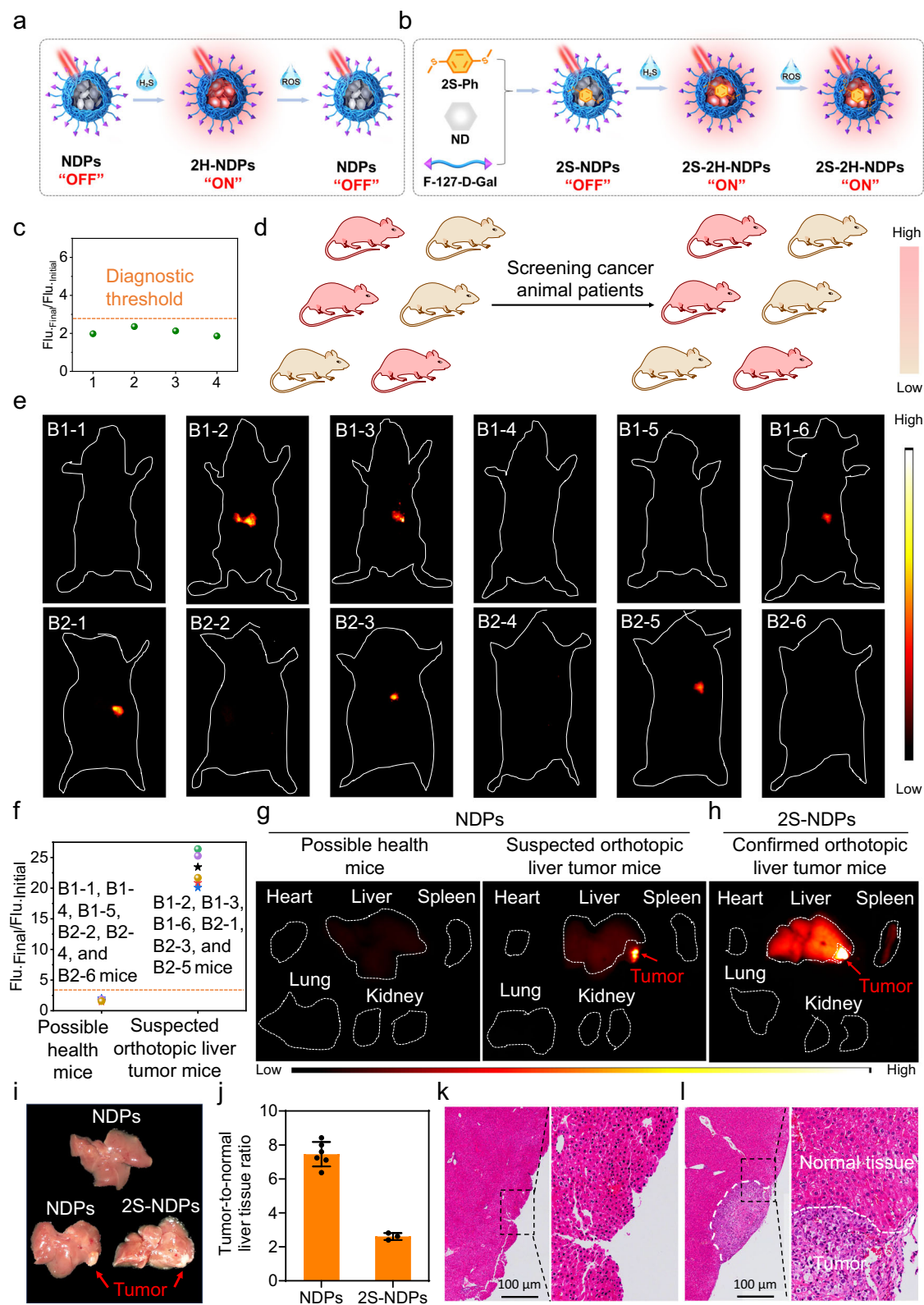
the diagnostic threshold. Therefore, these 6 mice were categorized into the 'suspected orthotopic liver tumor mice' group. The remaining 6 mice (B1-1 (1.71), B1-4 (1.49), B1-5 (2.01), B2-2 (1.71), B2-4 (1.85), B2-6 (1.56) mice) were categorized into the 'possible health mice' group (Fig. 6f). To further verify the accuracy of screening cancer patients with orthotopic liver tumors, the mice were sacrificed and ex vivo main organs were collected for NIR-II fluorescence imaging. The liver tissue of the 'possible health mice' group showed no contrast enhancement

(Fig. 6g, left), but obvious contrast enhancement at the bottom right of the liver was observed for the 'suspected orthotopic hepatoma mice' group (Fig. 6g right). Meanwhile, the NIR-II fluorescence in tumor and normal liver tissue of the 2S-NDPs-treated confirmed orthotopic liver tumor mice also showed obvious enhancement (Fig. 6h). These images matched the macroscopic images of livers (Fig. 6i). The fluorescence intensities of the tumors were significantly stronger than that of other organs (Supplementary Fig. S34) and the tumor-to-normal liver tissue

Fig. 6 | A blind study to screen animal patients with an orthotopic liver tumor. Schematic illustration of the fluorescence change of (**a**) NDPs and (**b**) 2S-NDPs in the presence of H$_2$S and ROS. Created in BioRender. Jiajing, G. (2022) BioRender.com/m53h190. **c** The Flu.$_{Final}$/Flu.$_{Initial}$ in liver at 10 h post i.v. injection of NDPs (10 mg Kg^{-1}) in healthy mice ($n = 4$ mice). **d** Schematic illustration of the stratification of a patient group based on NIR-II fluorescence signal intensity in a blind study. Created in BioRender. Jiajing, G. (2022) BioRender.com/m53h190. **e** NIR-II fluorescence imaging of six mice at 10 h post i.v. injection of NDPs (10 mg Kg^{-1}). (**f**) Stratification based on established diagnostic threshold and NIR-II fluorescence turn-on of six mice after i.v. injection of NDPs. The values of the first batch of mice have been marked with stars to distinguish them from the second batch (spheres). **g** Representative ex vivo NIR-II fluorescence images of main organs resected from the NDPs-treated 'possible health mice' group and 'suspected orthotopic liver tumor mice' group. **h** Representative ex vivo NIR-II fluorescence images of main organs resected from the 2S-NDPs-treated the 'conformed orthotopic liver tumor mice' group. **i** Representative macroscopic images of the liver tissues resected from (**g**, **h**), respectively. **j** The tumor-to-normal liver tissue signal ratio of NDPs-treated 'suspected orthotopic hepatoma mice' and 2S-NDPs-treated 'conformed orthotopic liver tumor mice', ($n = 6$ biologically independent samples for NDPs; mean ± SD, $n = 3$ biologically independent samples for 2S-NDPs; mean ± SD). Representative H&E staining of the liver tissue slice of the (**k**) 'possible health mice' group and the (**l**) 'suspected orthotopic hepatoma mice' group.

ratios for B1-2, B1-3, B1-6, B2-1, B2-3 and B2-5 mice were 8.42, 6.37, 8.00, 7.24, 7.11, 7.60, respectively. The mean tumor-to-normal liver tissue ratio is 7.46 (Fig. 6j), exceeding the Rose criterion of 5. By contrast, the tumor-to-normal liver tissue ratio of 2S-NDPs is only 2.61 (Fig. 6j).

Finally, the gold standard H&E staining showed that the tissues of contrast enhancement were tumors (Fig. 6k, l). When the identity of the mice was revealed, it showed correct diagnosis with 100% confidence. It also demonstrates that our probe could reliably identify liver orthotopic tumor-bearing mice even across different batches. Additionally, as shown in Fig. 6g, the tumor size is very small (~4 mm). Such a small tumor is generally considered to be an early orthotopic HepG2 liver tumor, while well-established clinical imaging techniques (such as CT, MRI, and US) can only detect liver tumors >10 mm (Supplementary Fig. S35)[83]. Conclusively, NDPs could accurately and non-invasively screen animal patients with orthotopic liver tumor and sensitively detected early and small orthotopic liver tumor through NIR-II fluorescence imaging of H$_2$S.

Biosafety evaluation of NDPs

Standard 3-(4,5-dimethyl-2-thiazolyl)-2,5-diphenyl-2-tetrazolium bromide analysis revealed no obvious cytotoxicity of NDPs even at the concentration of up to 1000 µg mL^{-1} (Supplementary Fig. S36). Next, in vivo toxicology was investigated systematically at a dosage of 50 mg Kg^{-1}. The body weight of mice injected with NDPs exhibited no significant difference compared with control mice without any treatment over a 30-d period (Supplementary Fig. S37). The hematological indexes at time points of 1, 7, and 30 d post-injection of NDPs showed negligible difference with the control mice (Supplementary Fig. S38), demonstrating that NDPs caused no obvious inflammation or infection. Moreover, the blood biochemical assay also showed no significant difference between the NDPs-treated mice and the control (Supplementary Fig. S39), demonstrating no nephrotoxicity, hepatotoxicity, or hematological toxicity. Haematoxylin and eosin-stained images of major organs presented no apparent histological abnormalities or lesions (Supplementary Fig. S40). All these data collectively indicate that NDPs are safe to use in vivo.

Discussion

Many life-threatening disease patients face poor survival primarily due to late-stage identification and missing optimal therapy windows because of delayed identification. Sensitive identification of early lesions is effective but heavily dependent on the disease tissue-to-normal tissue signal ratio of imaging probes. Exceeding the Rose criterion, which requires a signal-to-background ratio of 5 for 100% certain identification of image features, indicates the ability to distinguish disease tissues from healthy ones with absolute certainty[60–63]. However, while many probes exhibit ratios >5, attention to high signals in normal tissues has been lacking in most of these proof-of-concept studies. This oversight could lead to false positive or negative diagnoses in clinical settings. Notably, certain tissues pose a greater challenge, such as liver disease tissue imaging. Here, a ratio above 2 is often considered crucial for early tumor detection[64] to identify as many early

suspected tumor tissues as possible. As excessively high normal tissue signals can obscure these lesions, even when they genuinely exist but remain undetectable. Moreover, high normal tissue signal complicates the boundary distinction between diseased and healthy tissue. Therefore, developing probes with minimal or absent normal tissue signals is imperative for sensitive imaging of early tiny lesions. So far, "off-on" probes are the best strategy to reduce background signals. However, once the traditional "off-on" probes are activated in disease tissues and transformed into "always-on" probes, they gradually migrate from the disease tissues to normal tissues and lead to relatively high normal tissue signals. In this regard, "off-on-off" probes that could turn off their signals upon migration from the disease tissues to normal tissues are highly desirable, especially for liver tumor imaging.

In this study, we developed NIR-II-excited "off-on-off" NIR-II fluorescent probes (NDPs) with near-ideal zero initial probe fluorescence. The NDPs possess several unique properties that are advantageous over traditional "off-on" probes for highly sensitive molecular imaging in vivo: (1) Different from traditional "off-on" probe design based on photophysical processes to quench and revive fluorescence, such as aggregation-induced emission, photoinduced electron transfer, and fluorescence Forster resonance energy transfer, our probe design strategy is based on the large red-shift in probe absorbance before and after activation, which offers near-ideal zero pristine probe fluorescence in normal tissues, (2) favorable 1064 nm excitation and NIR-II emission to increase tissue penetration depth with negligible liver tissue autofluorescence[25], (3) "off-on-off" NIR-II fluorescence with the ability to lose signal upon migration from tumors to normal tissues, and (4) an ultrahigh fluorescence turn-on ratio of ~12000-fold in response of H$_2$S to increase the tumor signal. These advantages offer high molecular imaging sensitivity, which allowed us to noninvasively identify mice with orthotopic liver tumors from mixed subjects of healthy and tumor mice with 100% accuracy in tumor screening. In addition, NDPs could accurately locate early tumors with sizes as small as 4 mm, which is superior to those well-established clinical imaging techniques (such as CT, MRI, and US) that only can detect liver tumors >10 mm. Our probe design concept not only offers a promising molecular design blueprint for broad applicability in detecting and localizing early lesions with high sensitivity, but also holds the potential to further expand into therapeutic applications, aimed at reducing side effects and enhancing biosafety in treatments.

Methods

The research presented here complies with all relevant ethical regulations. All experiments involving animals were reviewed and approved (IACUC-003-9) by the guidelines of the Laboratory Animal Center of Jiangsu KeyGEN BioTECH Corp., Ltd., prior to commencing the study. All the maximal tumor size/burden in our experiments did not exceed the maximal tumor size/burden permitted (2000 mm^3) by the Laboratory Animal Center of Jiangsu KeyGEN BioTECH Corp., Ltd. The all cells, including HepG-2 cells, 3T3 cells and HEK 293 T cells, were reviewed the Jiangsu KeyGEN BioTECH Corp., Ltd. The materials and methods used in this study are described in detail in Supplementary

information, including descriptions of NIR-II fluorescent probes used in this study, NIR-II imaging method and consideration.

Preparation of NDPs

A microfluidic glass capillary mixer was used to prepare NDPs through modified nanoprecipitation with mixed solvents (Supplementary Fig. 6). ND (0.1 mg) and F-127-D-Gal (10 mg) were dissolved in tetrahydrofuran (THF, 1 mL). Deionized (D.I.) water (10 mL) was used as the antisolvent. The flow rate of THF and water was 10 and 100 mL min^{-1}. Then THF was evaporated at 60 °C. The rest of the aqueous solution was filtered through a 0.2 μm cellulose membrane filter to remove any precipitate before use. Then, the aqueous solution was washed three times using distilled-deionized water and centrifuged using 50 K centrifugal filter units (Millipore) at 136.975 xg for 10 min at 10 °C. Notably, the same method was used as above except for using Me-H-ND instead of ND. 2S-NDPs were achieved through nanoprecipitation with F127-D-Gal to encapsulate 1,4-bis(methylsulfanyl)benzene (2S-Ph) and ND in a molar ratio of 2 based on the same method.

Cell culture

Normal 3T3, HEK293T and human HCC HepG2 cells were purchased from Jiangsu KeyGEN BioTECH Corp., Ltd. and incubated respectively in DMEM supplemented with a medium containing 10% fetal bovine serum (FBS) and 1% penicillin/streptomycin at 37 °C in a humidified atmosphere of 5% CO_2.

In vivo NIR-II fluorescence imaging

The real-time in vivo NIR-II fluorescence imaging was performed using the home-built imaging set-up (CDD: NIRvana® 640, Teledyne Scientific & Imaging LLC). The excitation wavelength was fixed at a 1064 nm laser with laser energy of ~150 mW/cm^2 on the surface of mice or tissues. An 1100 nm long-pass filter (Thorlabs) was used to collect fluorescence.

In vivo NIR-II fluorescence imaging of subcutaneous liver tumors

Subcutaneous HepG2 tumor-bearing mice (~20 g) were divided into 3 groups and intravenously injected with a solution of NDPs (200 μL, 1 mg mL^{-1}) for in vivo NIR-II real-time fluorescence imaging. H_2S enhancer (L-Cys, 1 mM, 25 μL) or scavenger (AOAA, 1 mM, 25 μL) and saline (25 μL) were injected into tumors at 4 h before intravenous injection of NDPs.

Screening mice with orthotopic tumors from mixed subjects of healthy and tumor mice with a blind study

Establishment of a diagnostic threshold: Four healthy mice (~5–6 weeks old) were intravenously injected with NDPs (10 mg Kg^{-1}) to perform NIR-II fluorescence imaging. Then, the NIR-II fluorescence intensities in the liver at 10 h (Flu.$_{Final}$) and 0 h (Flu.$_{Initial}$) post i.v. injection of NDPs was recorded, respectively. The diagnostic threshold was defined as the mean value of Flu.$_{Final}$/Flu.$_{Initial}$ of four mice adding 2-fold of the s.d. value.

Screening mice with a blind study: We utilized two separate batches of mice from different time points to mitigate any potential batch effects. Each batch is consisted of six mice, and identical procedures were applied to both batches. The anterior abdominal wall of six nude mice (~5–6 weeks old) was made with a midline incision to expose the liver. These six mice were randomly divided into two groups. One of the groups was inoculated with HepG2 cells transfected with luciferase (10×10^6 in 20 μL DMEM) in their livers. The other group was treated with the same process except using normal saline instead of HepG2 cells. Bioluminescence imaging was used to monitor tumor growth. Then, all midline incisions of the two groups were stitched. The whole process ensures no biasing of the results based on the appearance of these six mice. After 15 days, the six mice were tagged and randomized by a second researcher, their identity was concealed until the

completion of the study. The NIR-II fluorescence intensities in the liver at 10 h (Flu.$_{Final}$) and 0 h (Flu.$_{Initial}$) post i.v. injection of NDPs was recorded, respectively. If the Flu.$_{Final}$/Flu.$_{Initial}$ value of a mouse is greater than the diagnostic threshold, it is not a healthy mouse but a suspected orthotopic HepG2 cancer patient.

Reporting summary

Further information on research design is available in the Nature Portfolio Reporting Summary linked to this article.

Data availability

All data generated or analyzed during this study are included in this article, its Supplementary information files, and source data files. All other data are available from the corresponding authors upon request. Source data are provided with this paper.

References

1. Owens, E. A., Henary, M., El Fakhri, G. & Choi, H. S. Tissue-specific near-infrared fluorescence imaging. *Acc. Chem. Res.* **49**, 1731–1740 (2016).
2. Cheng, D. et al. De novo design of chemical stability near-infrared molecular probes for high-fidelity hepatotoxicity evaluation in vivo. *J. Am. Chem. Soc.* **141**, 6352–6361 (2019).
3. Zhong, Y. et al. In vivo molecular imaging for immunotherapy using ultra-bright near-infrared-IIb rare-earth nanoparticles. *Nat. Biotechnol.* **37**, 1322–1331 (2019).
4. Chan, J., Dodani, S. C. & Chang, C. J. Reaction-based small-molecule fluorescent probes for chemoselective bioimaging. *Nat. Chem.* **4**, 973–984 (2012).
5. Hao, L. et al. Microenvironment-triggered multimodal precision diagnostics. *Nat. Mater.* **20**, 1440–1448 (2021).
6. Wu, L., Huang, J., Pu, K. & James, T. D. Dual-locked spectroscopic probes for sensing and therapy. *Nat. Rev. Chem.* **5**, 406–421 (2021).
7. Tang, Y. et al. Dual lock-and-key"-controlled nanoprobes for ultra-high specific fluorescence imaging in the second near-infrared window. *Adv. Mater.* **30**, e1801140 (2018).
8. Yu, M. & Zheng, J. Clearance pathways and tumor targeting of imaging nanoparticles. *ACS nano* **9**, 6655–6674 (2015).
9. Chen, Z. et al. Mammalian drug efflux transporters of the ATP binding cassette (ABC) family in multidrug resistance: a review of the past decade. *Cancer Lett* **370**, 153–164 (2016).
10. Kobayashi, H. & Choyke, P. L. Target-cancer-cell-specific activatable fluorescence imaging probes: rational design and in vivo applications. *Acc. Chem. Res.* **44**, 83–90 (2011).
11. Mi, P. et al. A pH-activatable nanoparticle with signal-amplification capabilities for non-invasive imaging of tumour malignancy. *Nat. Nanotech.* **11**, 724–730 (2016).
12. An, R., Wei, S., Huang, Z., Liu, F. & Ye, D. An activatable chemiluminescent probe for sensitive detection of gamma-glutamyl transpeptidase activity in vivo. *Anal. Chem.* **91**, 13639–13646 (2019).
13. Li, Y., Xue, C., Fang, Z., Xu, W. & Xie, H. In vivo visualization of gamma-glutamyl transpeptidase activity with an activatable self-immolating near-infrared probe. *Anal. Chem.* **92**, 15017–15024 (2020).
14. Yu, M. et al. Lysosomal pH decrease in inflammatory cells used to enable activatable imaging of inflammation with a sialic acid conjugated profluorophore. *Anal. Chem.* **87**, 6688–6695 (2015).
15. Wu, L. et al. Engineering of electrochromic materials as activatable probes for molecular imaging and photodynamic therapy. *J. Am. Chem. Soc.* **140**, 16340–16352 (2018).
16. Chen, N. et al. A lysosome specific, acidic-pH activated, near-infrared bodipy fluorescent probe for noninvasive, long-term, in vivo tumor imaging. *Mater. Sci. Eng. C* **111**, 110762 (2020).
17. Zhao, T. et al. A transistor-like pH nanoprobe for tumour detection and image-guided surgery. *Nat. Biomed. Eng.* **1**, 0006 (2016).

18. Tang, Y. et al. Organic semiconducting nanoprobe with redox-activatable NIR-II fluorescence for in vivo real-time monitoring of drug toxicity. *Chem. Commun.* **55**, 27–30 (2018).

19. Liu, Z. et al. A reversible fluorescent probe for real-time quantitative monitoring of cellular glutathione. *Angew. Chem. Int. Ed. Engl.* **56**, 5812–5816 (2017).

20. Zhang, Y. et al. Rational construction of a reversible arylazo-based NIR probe for cycling hypoxia imaging in vivo. *Nat. Commun.* **12**, 2772 (2021).

21. Umezawa, K., Yoshida, M., Kamiya, M., Yamasoba, T. & Urano, Y. Rational design of reversible fluorescent probes for live-cell imaging and quantification of fast glutathione dynamics. *Nat. Chem.* **9**, 279–286 (2016).

22. Urano, Y. et al. Selective molecular imaging of viable cancer cells with pH-activatable fluorescence probes. *Nat. Med.* **15**, 104–109 (2009).

23. Takahashi, S. et al. Reversible off-on fluorescence probe for hypoxia and imaging of hypoxia-normoxia cycles in live cells. *J. Am. Chem. Soc.* **134**, 19588–19591 (2012).

24. Zheng, J., Zeng, Q., Zhang, R., Xing, D. & Zhang, T. Dynamic-reversible photoacoustic probe for continuous ratiometric sensing and imaging of redox status in vivo. *J. Am. Chem. Soc.* **141**, 19226–19230 (2019).

25. Tang, Y., Pei, F., Lu, X., Fan, Q. & Huang, W. Recent advances on activatable NIR-II fluorescence probes for biomedical imaging. *Adv. Opt. Mater.* **7**, 1900917 (2019).

26. Wang, B. et al. A reversible fluorescence probe based on Se-BODIPY for the redox cycle between HClO oxidative stress and H2S repair in living cells. *Chem. Commun.* **49**, 1014–1016 (2013).

27. Zhou, Y. et al. Blood-brain barrier-penetrating siRNA nanomedicine for Alzheimer's disease therapy. *Sci. Adv.* **6**, eabc7031 (2020).

28. Pakhira, M., Chatterjee, D. P., Mallick, D., Ghosh, R. & Nandi, A. K. Reversible stimuli-dependent aggregation-induced emission from a "nonfluorescent" amphiphilic PVDF graft copolymer. *Langmuir* **37**, 4953–4963 (2021).

29. Ma, Y., Gao, W., Zhu, L., Zhao, Y. & Lin, W. Development of a unique reversible fluorescent probe for tracking endogenous sulfur dioxide and formaldehyde fluctuation in vivo. *Chem. Commun.* **55**, 11263–11266 (2019).

30. Hu, D. et al. Ultrasensitive reversible chromophore reaction of BODIPY functions as high ratio double turn on probe. *Nat. Commun.* **9**, 362 (2018).

31. Best, Q. A., Sattenapally, N., Dyer, D. J., Scott, C. N. & McCarroll, M. E. pH-dependent Si-fluorescein hypochlorous acid fluorescent probe: spirocycle ring-opening and excess hypochlorous acid-induced chlorination. *J. Am. Chem. Soc.* **135**, 13365–13370 (2013).

32. Zheng, S. et al. Radiopharmaceuticals and fluorescein sodium mediated triple-modality molecular imaging allows precise image-guided tumor surgery. *Adv. Sci.* **6**, 1900159 (2019).

33. Cao, C. et al. First clinical investigation of near-infrared window IIa/IIb fluorescence imaging for precise surgical resection of gliomas. *IEEE Trans. Biomed. Eng.* **69**, 2404–2413 (2022).

34. Cai, M., Zhang, Z., Shi, X., Hu, Z. & Tian, J. NIR-II/NIR-I fluorescence molecular tomography of heterogeneous mice based on gaussian weighted neighborhood fused lasso method. *IEEE Trans. Med. Imaging* **39**, 2213–2222 (2020).

35. Cai, M. et al. Non-negative iterative convex refinement approach for accurate and robust reconstruction in cerenkov luminescence tomography. *IEEE Trans. Med. Imaging* **39**, 3207–3217 (2020).

36. Chen, H. J. et al. An activatable and reversible virus-mimicking NIR-II nanoprobe for monitoring the progression of viral encephalitis. *Angew. Chem. Int. Ed. Engl.* **61**, e202210285 (2022).

37. Wang, S. et al. Anti-quenching NIR-II molecular fluorophores for in vivo high-contrast imaging and pH sensing. *Nat. Commun.* **10**, 1058 (2019).

38. Xiao, P. et al. De novo design of reversibly pH-switchable NIR-II aggregation-induced emission luminogens for efficient photo-theranostics of patient-derived tumor xenografts. *J. Am. Chem. Soc.* **145**, 334–344 (2023).

39. He, L. et al. Engineering of reversible NIR-II redox-responsive fluorescent probes for imaging of inflammation in vivo. *Angew. Chem. Int. Ed. Engl.* **61**, e202211409 (2022).

40. Liu, Y. et al. A reversible NIR-II ratiometric fluorescent probe for real-ideanne time in vivo ATP detection. *Adv. Opt. Mater.* **11**, 2301144 (2023).

41. Song, D., Li, C., Zhu, M., Chi, S. & Liu, Z. Tracking hepatic ischemia-reperfusion injury in real time with a reversible NIR-IIb fluorescent redox probe. *Angew. Chem. Int. Ed. Engl.* **61**, e202212721 (2022).

42. Zhao, M. et al. A tumor-microenvironment-responsive lanthanide-cyanine FRET sensor for NIR-II luminescence-lifetime in situ imaging of hepatocellular carcinoma. *Adv. Mater.* **32**, e2001172 (2020).

43. Sun, T. et al. Tailor-made semiconducting polymers for second near-infrared phototherapy of orthotopic liver cancer. *ACS nano* **13**, 7345–7354 (2019).

44. Lei, S. et al. A FRET-based ratiometric H(2)S sensor for sensitive optical molecular imaging in second near-infrared window. *Research* **6**, 0286 (2023).

45. Wu, L. et al. H2S-activatable near-infrared afterglow luminescent probes for sensitive molecular imaging in vivo. *Nat. Commun.* **11**, 446 (2020).

46. Wang, R. et al. Aggregation enhanced responsiveness of rationally designed probes to hydrogen sulfide for targeted cancer imaging. *J. Am. Chem. Soc.* **142**, 15084–15090 (2020).

47. Shi, D. T. et al. Selective fluorogenic imaging of hepatocellular H2S by a galactosyl azidonaphthalimide probe. *Chem. Commun.* **51**, 3653–3655 (2015).

48. Jose, D. A. et al. Sensing and bioimaging of the gaseous signaling molecule hydrogen sulfide by near-infrared fluorescent probes. *ACS Sensors* **5**, 3365–3391 (2020).

49. Ma, Y. et al. H2 S-activable MOF nanoparticle photosensitizer for effective photodynamic therapy against cancer with controllable singlet-oxygen release. *Angew. Chem. Int. Ed. Engl.* **56**, 13752–13756 (2017).

50. Shi, B. et al. Theranostic nanoplatform with hydrogen sulfide acti-vatable NIR responsiveness for imaging-guided on-demand drug release. *Angew. Chem. Int. Ed. Engl.* **58**, 16826–16830 (2019).

51. Xu, G. et al. Imaging of colorectal cancers using activatable nanoprobes with second near-infrared window emission. *Angew. Chem. Int. Ed. Engl.* **57**, 3626–3630 (2018).

52. Yang, C. T. et al. Data-driven identification of hydrogen sulfide scavengers. *Angew. Chem. Int. Ed. Engl.* **58**, 10898–10902 (2019).

53. Xie, J. et al. A NIR dye with high-performance n-type semi-conducting properties. *Chem. Sci.* **7**, 499–504 (2016).

54. Fu, L., Sun, C. & Yan, L. Galactose targeted pH-responsive copoly-mer conjugated with near infrared fluorescence probe for imaging of intelligent drug delivery. *ACS Appl. Mater. Interfaces* **7**, 2104–2115 (2015).

55. Lu, L. et al. Redox-responsive amphiphilic camptothecin prodrug nanoparticles for targeted liver tumor therapy. *J. Mater. Chem. B* **8**, 3918–3928 (2020).

56. Lv, F., Li, Y., Cao, B. & Liu, T. Galactose substituted zinc phthalo-cyanines as near infrared fluorescence probes for liver cancer imaging. *J. Mater. Sci. Mater. Med.* **24**, 811–819 (2013).

57. Li, B., Lu, L., Zhao, M., Lei, Z. & Zhang, F. An efficient 1064 nm NIR-II excitation fluorescent molecular dye for deep-tissue high-resolu-tion dynamic bioimaging. *Angew. Chem. Int. Ed. Engl.* **130**, 7605–7609 (2018).

58. Semonin, O. E. et al. Absolute photoluminescence quantum yields of IR-26 dye, PbS, and PbSe quantum dots. *J. Phys. Chem. Lett.* **1**, 2445–2450 (2010).

59. Cosco, E. D. et al. Flavylium polymethine fluorophores for near- and shortwave infrared imaging. *Angew. Chem. Int. Ed. Engl.* **56**, 13126–13129 (2017).

60. Bushberg, J. T., Boone, J. M. *The Essential Physics of Medical Imaging* 3rd edn, Vol. 1030 (Lippincott Williams & Wilkins, 2011).

61. Hong, G. et al. In vivo fluorescence imaging with Ag2S quantum dots in the second near-infrared region. *Angew. Chem. Int. Ed. Engl.* **51**, 9818–9821 (2012).

62. Lu, L. et al. NIR-II bioluminescence for in vivo high contrast imaging and in situ ATP-mediated metastases tracing. *Nat. Commun.* **11**, 4192 (2020).

63. Antaris, A. L. et al. A small-molecule dye for NIR-II imaging. *Nat. Mater.* **15**, 235–242 (2016).

64. Hu, Z. et al. First-in-human liver-tumour surgery guided by multispectral fluorescence imaging in the visible and near-infrared-I/II windows. *Nat. Biomed. Eng.* **4**, 259–271 (2020).

65. Zheng, X. et al. Hypoxia-specific ultrasensitive detection of tumours and cancer cells in vivo. *Nat. Commun.* **6**, 5834 (2015).

66. Jaeschke, H. & Ramachandran, A. Reactive oxygen species in the normal and acutely injured liver. *J. Hepatol.* **55**, 227–228 (2011).

67. Kannan, N. et al. Glutathione-dependent and -independent oxidative stress-control mechanisms distinguish normal human mammary epithelial cell subsets. *Proc. Natl. Acad. Sci. USA* **111**, 7789–7794 (2014).

68. Zhu, B. et al. Highly specific and ultrasensitive two-photon fluorescence imaging of native HOCl in lysosomes and tissues based on thiocarbamate derivatives. *Anal. Chem.* **88**, 12532–12538 (2016).

69. Feng, H. et al. A highly specific fluorescent probe for rapid detection of hypochlorous acidin vivoand in water samples. *J. Mater. Chem. B* **7**, 3909–3916 (2019).

70. Repenko, T. et al. Bio-degradable highly fluorescent conjugated polymer nanoparticles for bio-medical imaging applications. *Nat. Commun.* **8**, 470 (2017).

71. Jiang, Y. et al. Metabolizable semiconducting polymer nanoparticles for second near-infrared photoacoustic imaging. *Adv. Mater.* **31**, e1808166 (2019).

72. Stipanuk, M. H. & Beck, P. W. Characterization of the enzymic capacity for cysteine desulphhydration in liver and kidney of the rat. *Biochem. J.* **206**, 267–277 (1982).

73. Linden, D. R. et al. Production of the gaseous signal molecule hydrogen sulfide in mouse tissues. *J. Neurochem.* **106**, 1577–1585 (2008).

74. Abe, K. & Kimura, H. The possible role of hydrogen sulfide as an endogenous neuromodulator. *J. Neurosci.* **16**, 1066–1071 (1996).

75. Diao, S. et al. Biological imaging without autofluorescence in the second near-infrared region. *Nano Res.* **8**, 3027–3034 (2015).

76. Li, B., Lu, L., Zhao, M., Lei, Z. & Zhang, F. An efficient 1064 nm NIR-II excitation fluorescent molecular dye for deep-tissue high-resolution dynamic bioimaging. *Angew. Chem. Int. Ed. Engl.* **57**, 7483–7487 (2018).

77. An, L. et al. The in situ sulfidation of Cu2 O by endogenous H2 S for colon cancer theranostics. *Angew. Chem. Int. Ed. Engl.* **57**, 15782–15786 (2018).

78. Yin, C., Zhen, X., Fan, Q., Huang, W. & Pu, K. Degradable semiconducting oligomer amphiphile for ratiometric photoacoustic imaging of hypochlorite. *ACS nano* **11**, 4174–4182 (2017).

79. Zhang, J. et al. Activatable photoacoustic nanoprobes for in vivo ratiometric imaging of peroxynitrite. *Adv. Mater.* **29**, 1604764 (2016).

80. Hou, J.-T. et al. Sulfur-based fluorescent probes for HOCl: mechanisms, design, and applications. *Coord. Chem. Rev.* **450**, 214232 (2022).

81. Zheng, F. Y. et al. Development and application of G1-ELISA for detection of antibodies against bovine ephemeral fever virus. *Res. Vet. Sci.* **87**, 211–212 (2009).

82. Lucero, M. Y. & Chan, J. Photoacoustic imaging of elevated glutathione in models of lung cancer for companion diagnostic applications. *Nat. Chem.* **13**, 1248–1256 (2021).

83. Chen, Q. et al. H2O2-responsive liposomal nanoprobe for photoacoustic inflammation imaging and tumor theranostics via in vivo chromogenic assay. *Proc. Natl. Acad. Sci. USA* **114**, 5343–5348 (2017).

Acknowledgements

Author contributions

Y.F.T. and B.L. conceived and designed the study. Y.F.T., Y.Y.L., and C.X.H. performed all the experiments and the theoretical calculations. Y.F.T., Y.Y.L., C.X.H., W.H, Q.L.F and B.L. analyzed data and wrote the manuscript.

Competing interests

The authors declare no competing interests.

Additional information

Supplementary information The online version contains supplementary material available at https://doi.org/10.1038/s41467-024-55096-y.

Correspondence and requests for materials should be addressed to Quli Fan or Bin Liu.

Peer review information *Nature Communications* thanks the anonymous reviewers for their contribution to the peer review of this work. A peer review file is available.

Reprints and permissions information is available at http://www.nature.com/reprints

Publisher's note Springer Nature remains neutral with regard to jurisdictional claims in published maps and institutional affiliations.